NANO · MICRO small
www.small-journal.com

# Nanoscale Janus Z-Scheme Heterojunction for Boosting Artificial Photosynthesis

*Ke Su, Su-Xian Yuan, Li-Yuan Wu, Zhao-Lei Liu, Min Zhang,* and Tong-Bu Lu**

**Artificial photosynthesis for $CO_2$ reduction coupled with water oxidation currently suffers from low efficiency due to inadequate interfacial charge separation of conventional Z-scheme heterojunctions. Herein, an unprecedented nanoscale Janus Z-scheme heterojunction of $CsPbBr_3/TiO_x$ is constructed for photocatalytic $CO_2$ reduction. Benefitting from the short carrier transport distance and direct contact interface, $CsPbBr_3/TiO_x$ exhibits significantly accelerated interfacial charge transfer between $CsPbBr_3$ and $TiO_x$ ($8.90 \times 10^8$ $s^{-1}$) compared with $CsPbBr_3$:$TiO_x$ counterpart ($4.87 \times 10^7$ $s^{-1}$) prepared by traditional electrostatic self-assembling. The electron consumption rate of cobalt doped $CsPbBr_3/TiO_x$ can reach as high as $405.2 \pm 5.6$ μmol $g^{-1}$ $h^{-1}$ for photocatalytic $CO_2$ reduction to CO coupled with $H_2O$ oxidation to $O_2$ under AM1.5 sunlight (100 mW $cm^{-2}$), over 11-fold higher than that of $CsPbBr_3$:$TiO_x$, and surpassing the reported halide-perovskite-based photocatalysts under similar conditions. This work provides a novel strategy to boost charge transfer of photocatalysts for enhancing the performance of artificial photosynthesis.**

## 1. Introduction

The emission of tremendous $CO_2$ from excessive consumption of fossil energy has caused a series of climate and environmental problems.[1] Artificial photosynthesis is regarded as one of promising strategies to realize $CO_2$ recycle,[2] by directly utilizing inexhaustible solar energy to convert $CO_2$ and $H_2O$ into fuels or chemicals with the aid of photocatalysts,[3] as plants doing every day. An ideal carbon neutrality photocatalyst should simultaneously drive $CO_2$ reduction and water oxidation efficiently to achieve highly efficient $CO_2$ conversion.[4] However, most of the reported photocatalysts with visible light response for $CO_2$ photoreduction are inseparable from the employment of sacrificial reagents,[5] owing to the difficult energy-uphill reaction of water oxidation.[6] In fact, only a few semiconductors, such as $TiO_2$,[7] ZnO,[8] GaN,[9] $InVO_4$,[10] $Cu_2O$,[11] BiOBr[12] et. al can achieve photocatalytic $CO_2$ reduction using water as an electron donor, while the photoconversion efficiency is still far from satisfactory due to the low visible-light-harvesting capacity and/or fast photogenerated electron–hole recombination.[13] Thereby, the exploitation of photocatalyst with robust visible light response and highly efficient carrier separation is highly desired for artificial photosynthesis.

The construction of semiconductor heterojunctions is the most common strategy to improve the separation of photogenerated carries, which can effectively promote the performance of artificial photosynthesis. In particular, Z-scheme heterojunctions can not only improve the photogenerated carrier separation, but also retain the stronger oxidative and reductive capabilities of carriers (**Scheme 1**a), which have received widespread attention in the field of photocatalysis in recent years.[14] At present, there are two typical structures of Z-scheme heterojunctions. The most common one is composed of small semiconductor nanoparticles (SC-2) on bulky semiconductor substrate (SC-1) (Scheme 1b). In this type of Z-scheme heterojunctions, the interfacial contact area between SC-1 and SC-2 is very small, most of the photogenerated carriers in SC-1 recombine before reaching the interface of the heterojunction (Scheme 1b). The other one is consisted of two surface ligand-protected semiconductor nanoparticles (SC-1 and SC-2) assembled via electrostatic interactions. However, the surface-adsorbed ligands hinder the direct contact of two semiconductors (Scheme 1c), which is detrimental to the interfacial charge transfer and separation. Nanoscale Janus Z-scheme heterojunction has a short carrier transport distance and direct contact interface (Scheme 1d), which is beneficial for efficient transport and separation of photogenerated carriers. Moreover, compared with the traditional Z-scheme heterojunctions (Scheme 1b), nanoscale heterojunction has a larger light-harvesting area. As a result, nanoscale Janus Z-scheme heterojunction are expected to enhance the efficiency of $CO_2$ photoreduction. Nevertheless, to our knowledge, no such Z-scheme heterojunction has been investigated for photocatalytic $CO_2$ reduction thus far.

Herein, we report a metal-halide perovskite (MHP) based nanoscale Janus Z-scheme heterojunction of $CsPbBr_3/TiO_x$ through a facile interfacial synthesis method,[15] and employ

K. Su, S.-X. Yuan, L.-Y. Wu, Z.-L. Liu, M. Zhang, T.-B. Lu
MOE International Joint Laboratory of Materials Microstructure
Institute for New Energy Materials and Low Carbon Technologies
School of Materials Science and Engineering
Tianjin University of Technology
Tianjin 300384, China
E-mail: zm2016@email.tjut.edu.cn; lutongbu@tjut.edu.cn
M. Zhang
Tianjin Key Laboratory of Organic Solar Cells and Photochemical Conversion
School of Chemistry and Chemical Engineering
Tianjin University of Technology
Tianjin 300384, China
The ORCID identification number(s) for the author(s) of this article can be found under https://doi.org/10.1002/smll.202301192.

**DOI: 10.1002/smll.202301192**

 

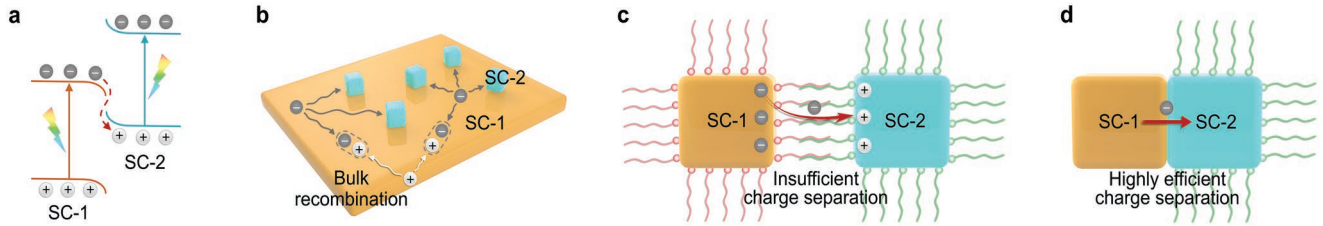


**Scheme 1.** a) The energy band structure and charge transfer pathway of a Z-scheme heterojunction. b,c) Two typical Z-scheme heterojunctions composed of b) small semiconductor nanoparticles (SC-2) on bulky semiconductor substrate (SC-1), and c) two surface ligand-protected semiconductor nanoparticles assembled via electrostatic interactions. d) Unprecedented Z-scheme heterojunction composed of nanoparticle with Janus configuration. SC-1 and SC-2 denote two different semiconductors.

it as a photocatalyst for efficient $CO_2$ reduction coupled with $H_2O$ oxidation. MHP nanocrystals (NCs) have been utilized in many fields such as photovoltaic[16] and optoelectronic devices[17] due to their excellent visible-light-harvesting capability and long photogenerated carrier lifetime,[18] which endow MHP NCs with a fascinating prospect for artificial photosynthesis.[19] $CsPbBr_3$ was in-situ formed from the transformation of $Cs_4PbBr_6$ NCs at the hexane/water interface.[20] During the transformation of $Cs_4PbBr_6$ to $CsPbBr_3$, the surface ligands of $CsPbBr_3$ NC facing the water side will be removed, which provide an opportunity for the deposition of titanium matrix ($TiO_x$) at the surface of $CsPbBr_3$ NC via in-situ hydrolysis of titanium butoxide (TBO) at the hexane/water interface, and $TiO_x$ can only grow along one side of $CsPbBr_3$,[15,21] resulting in the formation of nanoscale Janus heterojunction of $CsPbBr_3$/$TiO_x$. As expected, the as-prepared $CsPbBr_3/TiO_x$ heterojunction exhibits swift interfacial charge transfer, which endows $CsPbBr_3/TiO_x$ with a significantly enhanced photocatalytic activity for $CO_2$ reduction compared with $CsPbBr_3$:$TiO_x$ heterojunction prepared by traditional electrostatic self-assembling approach. Without any organic sacrificial agents, the electron consumption rate of cobalt doped $CsPbBr_3/TiO_x$ reaches as high as 405.2 ± 5.6 μmol $g^{-1}$ $h^{-1}$ for photocatalysis $CO_2$ reduction coupled with water oxidation under 1 sun irradiation, far surpassing the reported MHP-based photocatalysts under the similar conditions (Table S1, Supporting Information). As far as we know, it is the first MHP-based Z-scheme heterojunction with nanoscale Janus configuration toward artificial photosynthesis.

## 2. Results and Discussion

### 2.1. Preparation and Characterization of $CsPbBr_3/TiO_x$ Heterojunction

The synthesis process of $CsPbBr_3/TiO_x$ heterojunction is illustrated in Scheme S1, Supporting Information, and the detailed recipes are described in the Experimental Section. Briefly, monodispersed $Cs_4PbBr_6$ NCs (Figure S1, Supporting Information) prepared by a hot-injection method were firstly dispersed in hexane. Then, the colloidal $Cs_4PbBr_6$ hexane solution was mixed with TBO under stirring, followed by quickly injecting a small amount of deionized water into the mixture. After vigorous stirring for 5 min, the mixture was kept unperturbed at room temperature for 12 h. During this process, the color of the solution changed from initial colorless to bright green, and then gradually changed to yellow (Figure S2, Supporting Information). This phenomenon indicates the occurrence of chemical transformation from $Cs_4PbBr_6$ to $CsPbBr_3$ through stripping out CsBr from $Cs_4PbBr_6$ at the hexane/water interface, owing to the high solubility of CsBr in water.[20]

The chemical transformation can be further demonstrated by monitoring the absorption spectra. As depicted in Figure S3, Supporting Information, in contrast to initial solution showing three characteristic absorption peaks of $Cs_4PbBr_6$ NCs (206, 233, and 313 nm), the final yellow solution exhibits three new absorption peaks at 216, 270, and 510 nm, suggesting the generation of $CsPbBr_3$ NCs. The sharp absorption peaks of $Cs_4PbBr_6$ NCs are not observed for the final solution, indicating the complete transformation from $Cs_4PbBr_6$ to $CsPbBr_3$. Meanwhile, the extraction of CsBr from $Cs_4PbBr_6$ in the hexane/water interface would be accompanied by the removal of surface ligands on $CsPbBr_3$ NCs facing the water side, which allows the nucleation and growth of in-situ generated titanium matrix ($TiO_x$) at the interface through the hydrolysis of TBO to construct nanoscale Janus $CsPbBr_3/TiO_x$ heterojunction (Scheme S1, Supporting Information).

Transmission electron microscopy (TEM) was employed to investigate the morphology and composition of $CsPbBr_3$/$TiO_x$. As presented in **Figure 1**a, nanoscale Janus $CsPbBr_3$/$TiO_x$ heterojunction can be clearly observed, and each $CsPbBr_3$/$TiO_x$ heterojunction is composed of two separated components. $CsPbBr_3$ displays a cubic morphology, which is different from $Cs_4PbBr_6$ with a quasi-spherical morphology (Figure S1, Supporting Information). The average size of $CsPbBr_3$ NCs in $CsPbBr_3/TiO_x$ is 13.5 nm (Figure S4, Supporting Information), which is smaller than that of initial $Cs_4PbBr_6$ NCs (15.5 nm, Figure S1, Supporting Information). In addition, dynamic light scattering (DLS) measurements of pure $Cs_4PbBr_6$ and $CsPbBr_3$ NCs also showed that the average particle size of $CsPbBr_3$ is ≈2 nm smaller than that of $Cs_4PbBr_6$ (Figure S5, Supporting Information). The size shrinkage of $CsPbBr_3$ NCs can be attributed to CsBr-stripping during the transformation process. The small black dots on the surface of $CsPbBr_3$ (Figure 1a) should be Pb particles formed by high-energy electron irradiation during the TEM measurement, which has been commonly observed in previous reports.[22] High-resolution TEM (HRTEM) image (Figure 1b) exhibits distinct lattice spacing of 0.58 nm, which can be assigned to the (100) lattice plane of cubic $CsPbBr_3$ in $CsPbBr_3/TiO_x$, being consistent with that of $CsPbBr_3$ obtained by identical condition without adding TBO

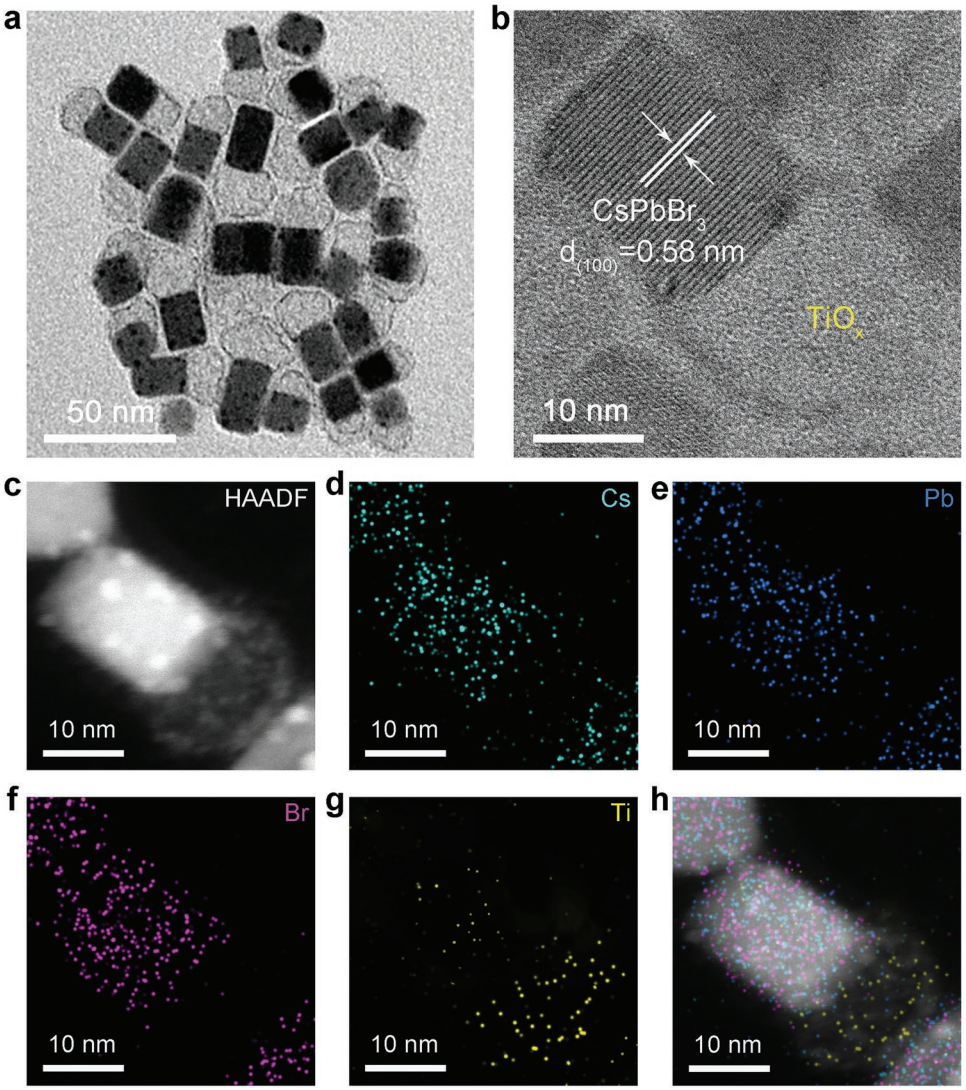


**Figure 1.** a) TEM image of $CsPbBr_3/TiO_x$. b) HRTEM image labeling the lattice spacing of $CsPbBr_3/TiO_x$. c) HAADF-STEM image, and d–h) elemental mapping images of $CsPbBr_3/TiO_x$: d) Cs; e) Pb; f) Br; g) Ti; h) overlap.

precursor (Figure S6, Supporting Information). There is no unambiguous lattice spacing in the light part (≈16 nm in size) of $CsPbBr_3/TiO_x$ heterojunction, indicating the in situ generated $TiO_x$ is amorphous, which is in accordance with previously reported $TiO_x$ based on the hydrolysis reaction of TBO at room temperature.[21] High-angle annular dark-field scanning TEM (HAADF-STEM) and energy-dispersive X-ray spectroscopy (EDS) mapping measurements were further carried out to inspect the elemental distribution of $CsPbBr_3/TiO_x$. As shown in Figure 1c–h, Cs, Pb, and Br are concentrated on the one side, while titanium element mainly appears on the other side, further conforming the formation of a nanoscale Janus $CsPbBr_3/TiO_x$ heterojunction. It is worth noting that the morphology of $CsPbBr_3/TiO_x$ heterojunction is significantly different from that of $CsPbBr_3$:$TiO_x$ heterojunction (made from the mixture of $CsPbBr_3$ and $TiO_x$ nanocrystals, see details in the Supporting Information), in which most of $CsPbBr_3$ and $TiO_x$ nanoparticles have separated from each other (Figure S7, Supporting Information), owing to the hindrance of long alkyl chain ligands on the surface of $CsPbBr_3$ nanocrystals.

The powder X-ray diffraction (PXRD) measurements were further performed to inspect the structure of $CsPbBr_3/TiO_x$. As depicted in **Figure 2**a, $CsPbBr_3$ exhibits distinct characteristic diffraction peaks at 15.0°, 21.4°, 30.4°, and 37.6°, which can be assigned to (100), (110), (200), and (211) facets of $CsPbBr_3$ with cubic phase (JCPDS: 00–054–0752), respectively. The XRD pattern of $CsPbBr_3/TiO_x$ also contains the characteristic diffraction peaks indexed to cubic phase $CsPbBr_3$, and no typical signals of $Cs_4PbBr_6$ can be observed, further demonstrating the complete chemical transformation from $Cs_4PbBr_6$ to $CsPbBr_3$ during the formation of $CsPbBr_3/TiO_x$. In addition, there are no $TiO_x$ characteristic peaks in the XRD pattern of $CsPbBr_3/TiO_x$ due to the amorphous structure of $TiO_x$, as confirmed by the result of pure $TiO_x$ prepared by the same method (Figure S8, Supporting Information). The presence of $TiO_x$ in $CsPbBr_3/TiO_x$ composite was demonstrated by Fourier transform infrared (FTIR)

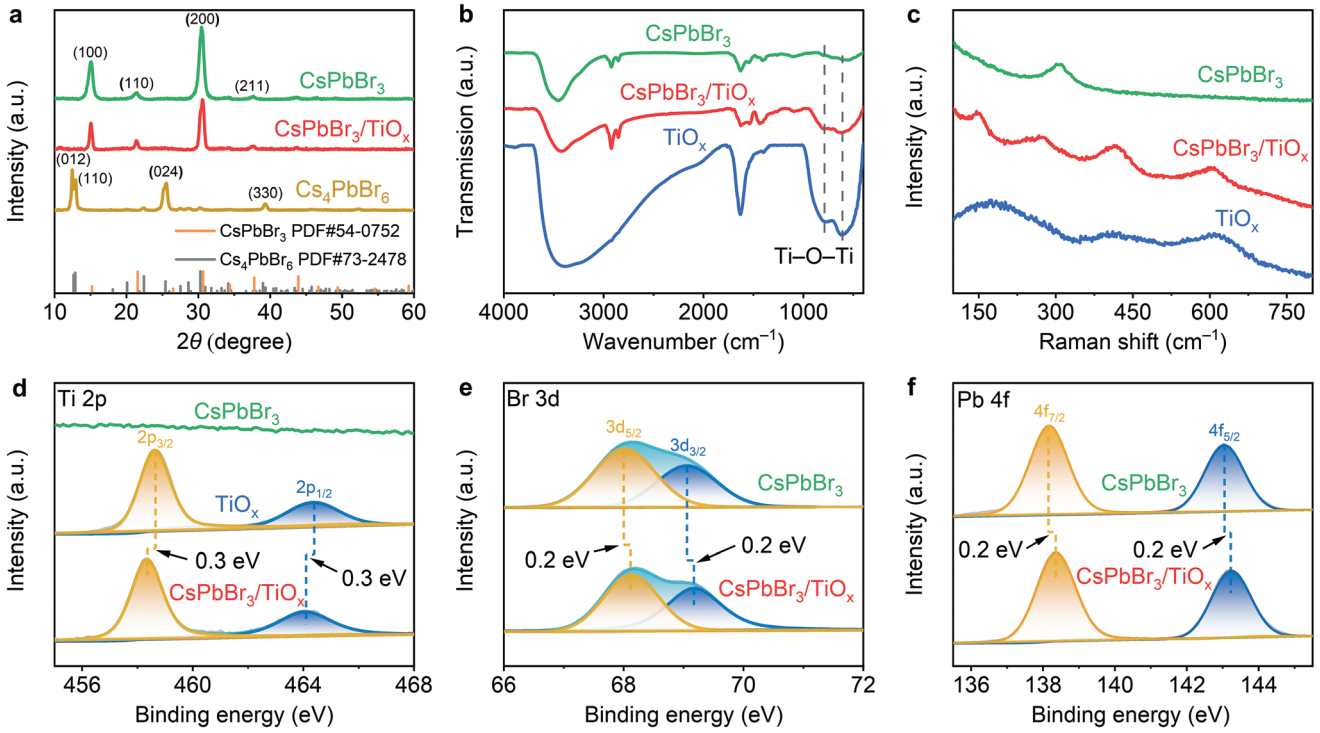


**Figure 2.** a) PXRD patterns of $CsPbBr_3$, $CsPbBr_3/TiO_x$, and $Cs_4PbBr_6$. b) FTIR, and c) Raman spectra of $TiO_x$, $CsPbBr_3$, and $CsPbBr_3/TiO_x$. High-resolution XPS spectra of d) Ti 2p in $TiO_x$, $CsPbBr_3$ and $CsPbBr_3/TiO_x$, e) Br 3d and f) Pb 4f in $CsPbBr_3$ and $CsPbBr_3/TiO_x$.

spectroscopy, Raman spectroscopy, and X-ray photoelectron spectroscopy (XPS) measurements. As shown in Figure 2b, apart from the characteristic peaks of $CsPbBr_3$, the FTIR spectrum of $CsPbBr_3/TiO_x$ shows strong Ti–O–Ti vibration peaks at 780 and 610 $cm^{-1}$.[23] In addition, both the Raman signals for $TiO_x$ (413 and 602 $cm^{-1}$)[24] and $CsPbBr_3$ (306 $cm^{-1}$)[25] can be clearly observed in $CsPbBr_3/TiO_x$ (Figure 2c). Moreover, in contrast to pure $CsPbBr_3$, two new peaks at 458.3 and 464.1 eV assigned to Ti $2p_{3/2}$ and Ti $2p_{1/2}$ for $Ti^{4+}$–O bonds[26] can be clearly observed in high-resolution XPS spectrum of $CsPbBr_3/TiO_x$ composite as shown in Figure 2d. Furthermore, there are perceptible shifts of binding energies for Ti 2p (Figure 2d) and Br 3d, Pb 4f, Cs 3d (Figure 2e, Figure 2f, and Figure S9, Supporting Information) in $CsPbBr_3/TiO_x$ in comparison with those in individual $TiO_x$ and $CsPbBr_3$, suggesting a strong electronic coupling between $CsPbBr_3$ and $TiO_x$ due to the tight contact between $CsPbBr_3$ and $TiO_x$ in $CsPbBr_3/TiO_x$ heterojunction.

### 2.2. Interfacial Charge Transfer Dynamics of $CsPbBr_3/TiO_x$ Heterojunction

Considering that the band alignment of the heterojunction plays a crucial role in determining the interfacial electron transfer and the thermodynamic feasibility of photocatalytic reaction, we first resorted to the UV–visible diffuse reflectance spectroscopy (UV–Vis DRS) and ultraviolet photoelectron spectroscopy (UPS) measurements to obtain the electronic band alignments of $CsPbBr_3$ and $TiO_x$. As presented in **Figure 3**a, the absorption edges of pure $CsPbBr_3$ and $TiO_x$ are ≈537 and 377 nm, respectively, which also can be clearly observed in $CsPbBr_3/TiO_x$ composite. According to the corresponding Tauc plots (Figure S10, Supporting Information), the optical bandgaps ($E_G$) of $CsPbBr_3$ and $TiO_x$ can be determined to be 2.36 and 3.11 eV, respectively, which are consistent with the reported values for $CsPbBr_3$[27] and $TiO_x$.[14e] Figure 3b–c display the UPS spectra of $CsPbBr_3$ and $TiO_x$, from which the valence band edge potentials ($E_{VB}$) of $CsPbBr_3$ and $TiO_x$ can be calculated as 1.73 and 2.74 V versus the standard hydrogen electrode (SHE), respectively. In combination with the values of $E_G$ and $E_{VB}$, we can deduce the conduction band potentials ($E_{CB}$) of $CsPbBr_3$ and $TiO_x$, being –0.63 and –0.37 V versus SHE, respectively. Thereby, the $CsPbBr_3/TiO_x$ heterojunction should display a staggered band alignment as illustrated in Figure 3d.

The dynamics of photogenerated carriers in $CsPbBr_3/TiO_x$ heterojunction was further scrutinized by steady-state and transient photoluminescence (PL) measurements. The excitation wavelength was selected at 450 nm to avoid the absorption of $TiO_x$. As shown in Figure 3e, individual $CsPbBr_3$ possesses a strong PL emission with a characteristic peak at 517 nm. There is an insignificant reduced PL intensity in the $CsPbBr_3$:$TiO_x$ composite, indicating the sluggish electron transfer between $CsPbBr_3$ and $TiO_x$ because of their separated structure (Figure S7, Supporting Information). It is worth noting that $CsPbBr_3/TiO_x$ heterojunction exhibits dramatical PL quenching, revealing the unique benefit of nanoscale Janus heterojunction for interfacial charge transfer. The time-resolved PL (TRPL) measurements further demonstrated that the nanoscale Janus heterojunction is beneficial to interfacial charge separation. As presented in Figure 3f, the TRPL trace of pure $CsPbBr_3$ NCs denotes the dynamic process of exciton

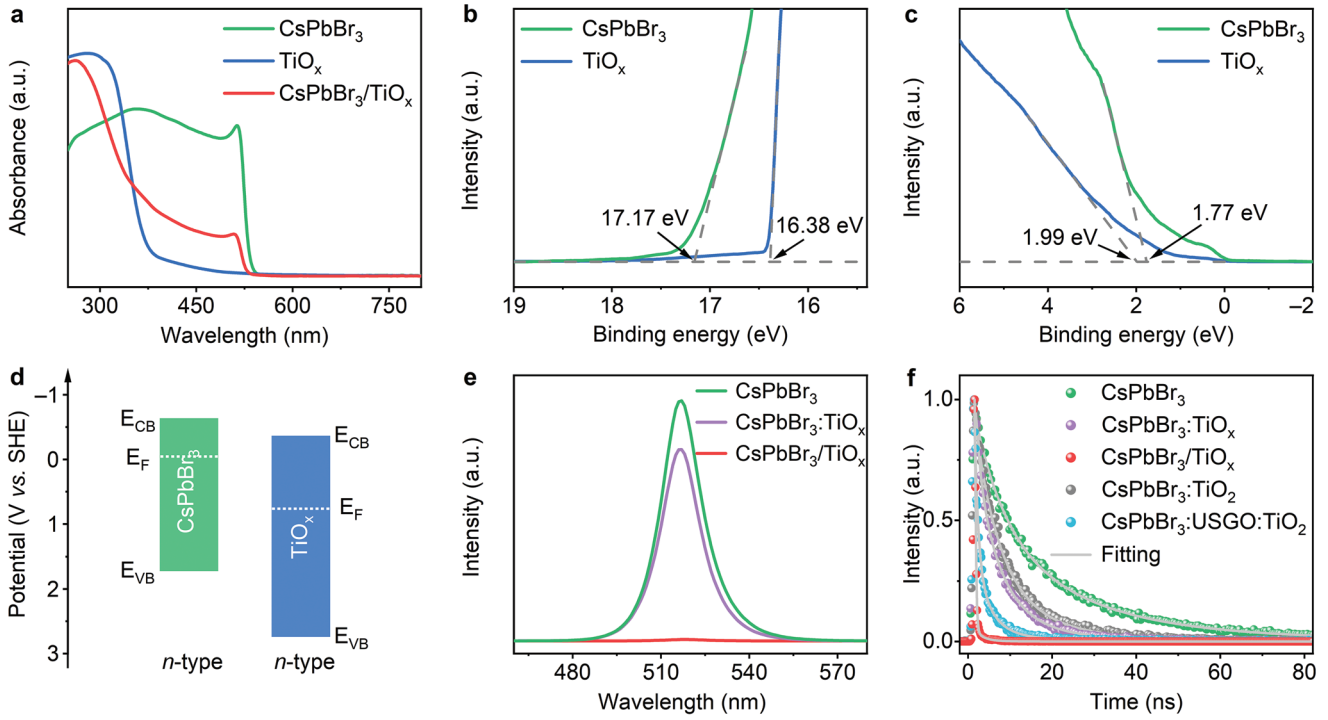


**Figure 3.** a) UV–Vis DRS spectra of $TiO_x$, $CsPbBr_3$, and $CsPbBr_3/TiO_x$. UPS of as-prepared $CsPbBr_3$ and $TiO_x$ in the b) cutoff and c) onset energy regions. d) Energy band diagrams of $CsPbBr_3$ and $TiO_x$ before contact. e) Steady-state PL of $CsPbBr_3$, $CsPbBr_3$:$TiO_x$ and $CsPbBr_3/TiO_x$. f) Time-correlated PL decay traces of $CsPbBr_3$, $CsPbBr_3$:$TiO_x$, $CsPbBr_3/TiO_x$, $CsPbBr_3$:$TiO_2$ and $CsPbBr_3$:USGO:$TiO_2$.

deactivation in $CsPbBr_3$ by combining radiative and nonradiative pathways, and the PL average lifetime of $CsPbBr_3$ NCs can be calculated to be 27.94 ns by fitting the corresponding TRPL trace with a multiexponential function (see more details in Table S2, Supporting Information). Compared to individual $CsPbBr_3$ NCs, $CsPbBr_3$:$TiO_x$ composite features a degree of accelerated PL decay with a shortened PL average lifetime of 11.83 ns, which indicates the occurrence of interfacial charge transfer in $CsPbBr_3$:$TiO_x$ owing to the energy off-set between $CsPbBr_3$ and $TiO_x$. In sharp contrast, the PL decay in $CsPbBr_3/TiO_x$ heterojunction was significantly accelerated, indicating that swift charge transfer occurred at the interface of $CsPbBr_3/TiO_x$ heterojunction. The corresponding PL average lifetime is remarkably reduced to 1.08 ns, which is significantly shorter than those of pristine $CsPbBr_3$ NCs and $CsPbBr_3$:$TiO_x$ composite. The corresponding interfacial charge transfer rate constants in $CsPbBr_3/TiO_x$ and $CsPbBr_3$:$TiO_x$ heterojunctions can be derived to be $8.90 \times 10^8$ and $4.87 \times 10^7$ $s^{-1}$, respectively.

The surface photovoltage (SPV) measurements were further carried out to substantiate the favorable impact of nanoscale Janus heterojunction on the transport and separation of photogenerated carriers. Upon light illumination, in general, the more negative change of SPV signal means the more accumulation of photogenerated electrons on the surface of semiconductor.[28] Pure $TiO_x$ shows negligible SPV response under light irradiation (Figure S11, Supporting Information), owing to the weak light-harvesting capacity and rapid electron–hole recombination of $TiO_x$.[29] Benefiting from the strong light absorption and long photogenerated carrier lifetime, sole $CsPbBr_3$ NCs exhibit obviously negative change of ≈50 mV (**Figure 4**). Notably, $CsPbBr_3/TiO_x$ nanoparticles display dramatic change of SPV signal (≈200 mV) as shown in Figure 4, which is also significantly larger than that of $CsPbBr_3$:$TiO_x$ composite (≈60 mV, Figure S12, Supporting Information). Apparently, $CsPbBr_3/TiO_x$ heterojunction with a close contact interface can facilitate interfacial charge separation to achieve high concentration of photogenerated carriers on the surface of semiconductor, which can be further confirmed by the photoelectrochemical measurements. As presented in Figure S13a, Supporting Information, $CsPbBr_3/TiO_x$ exhibits a significantly larger photocurrent density with respect to individual $CsPbBr_3$ and $CsPbBr_3$:$TiO_x$ composite. In addition, the Nyquist semicircle diameter of $CsPbBr_3/TiO_x$ nanoparticles is also noticeably smaller than those of $CsPbBr_3$ and $CsPbBr_3$:$TiO_x$ composite (Figure S13b and Table S3, Supporting Information).

### 2.3. Photocatalytic $CO_2$ Reduction Activity of $CsPbBr_3/TiO_x$ Heterojunction

The photoreduction $CO_2$ performance of $CsPbBr_3/TiO_x$ was evaluated in a gas–solid reaction apparatus in the presence of $H_2O$ vapor. A solar simulator with the light intensity of 100 mW $cm^{-2}$ was employed to simulate AM1.5 sunlight. The individual $CsPbBr_3$ and $TiO_x$ as well as $CsPbBr_3$:$TiO_x$ composite were also assessed to corroborate the merit of nanoscale Janus configuration in photocatalytic activity under the same condition. The major reduction product was identified as CO by chromatographic analyses for all the samples, and no

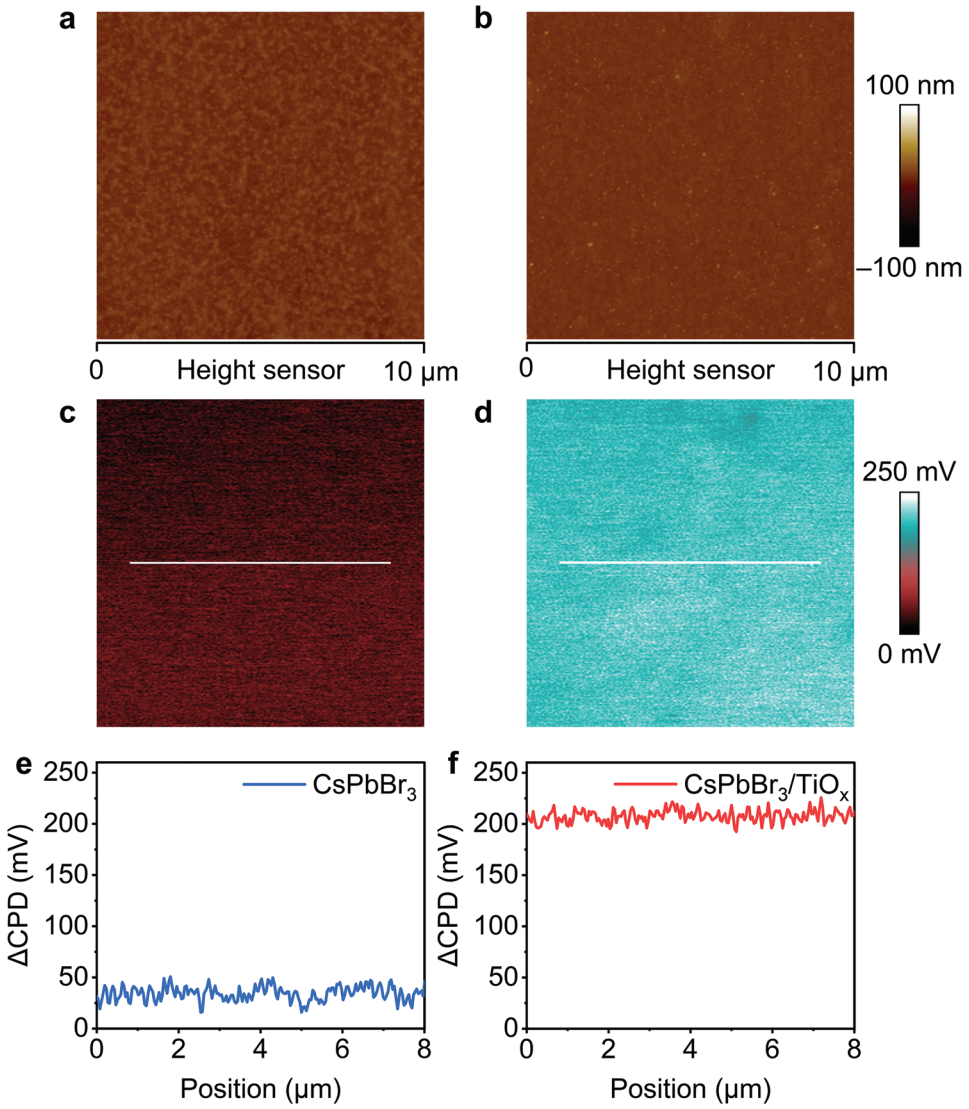


**Figure 4.** Height images of a) $CsPbBr_3$ and b) $CsPbBr_3/TiO_x$. The differential SPV images of c) $CsPbBr_3$ and d) $CsPbBr_3/TiO_x$ between potential images under illumination and in the dark. Contact potential difference changes (ΔCPD) of e) $CsPbBr_3$ and f) $CsPbBr_3/TiO_x$ by subtracting the potential in the dark conditions from that under illumination.

other unignorable reduction product can be detected. The CO generation rates for all the photocatalysts were visualized in **Figure 5**a. $TiO_x$ alone displays very inferior activity for photocatalytic $CO_2$ reduction due to its weak visible light capture ability, with a CO generation rate of only $4.1 \pm 1.4$ μmol $g^{-1}$ $h^{-1}$. Despite $CsPbBr_3$ possesses good visible light response, pristine $CsPbBr_3$ also exhibits very low CO generation rate ($8.0 \pm 1.3$ μmol $g^{-1}$ $h^{-1}$), which can be ascribed to the lack of activity sites and the weak water oxidation ability. Combining $CsPbBr_3$ and $TiO_x$ through electrostatic self-assembly ($CsPbBr_3$:$TiO_x$) only slightly improves the performance of photoreduction $CO_2$, exhibiting a marginally higher CO generation rate of $18.2 \pm 1.7$ μmol $g^{-1}$ $h^{-1}$. This result should be attributed to the fact that the presence of long alkyl chain ligands on the surface of $CsPbBr_3$ hindered the direct contact between the $CsPbBr_3$ and $TiO_x$ (Figure S7, Supporting Information), resulting in insufficient separation of photogenerated carriers.[30]

In sharp contrast, nanoscale Janus $CsPbBr_3/TiO_x$ heterojunction possesses swift interfacial electron transfer and thus efficient charge separation, which endows $CsPbBr_3/TiO_x$ with a remarkably enhanced performance for $CO_2$ photoreduction. The average CO generation rate of $CsPbBr_3/TiO_x$ is $108.5 \pm 2.4$ μmol $g^{-1}$ $h^{-1}$ (Figure 5a), which is ≈14, 26, and 6 times higher than those of $CsPbBr_3$, $TiO_x$, and $CsPbBr_3$:$TiO_x$, respectively. To evaluate the superiority of nanoscale Janus Z-scheme heterojunction in photocatalytic activity, the currently developed MHP-based heterostructures, including direct Z-scheme heterojunction $CsPbBr_3$:$TiO_2$ (loading $CsPbBr_3$ nanoparticles on large-size $TiO_2$ substrate), and all-solid-state Z-scheme heterojunction $CsPbBr_3$:USGO:$TiO_2$ (loading $CsPbBr_3$ nanocrystals and $TiO_2$ nanofibers on the ultrathin small-size graphene oxide (USGO) electron mediator), were also prepared as references. As shown in Figure 5a, The CO generation rates of $CsPbBr_3$:$TiO_2$ and $CsPbBr_3$:USGO:$TiO_2$

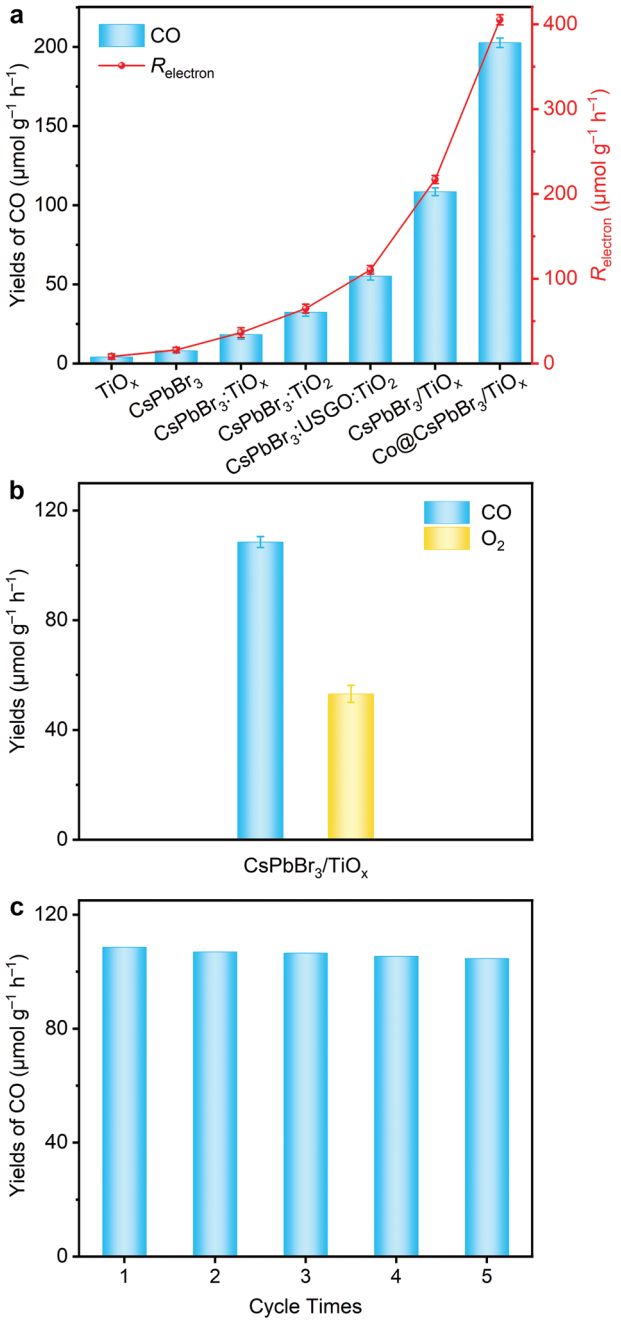


**Figure 5.** a) Yields of CO and corresponding total electron consumption rates ($R_{electron}$), with TiO$_x$, CsPbBr$_3$, CsPbBr$_3$:TiO$_x$, CsPbBr$_3$:TiO$_2$, CsPbBr$_3$:USGO:TiO$_2$, CsPbBr$_3$/TiO$_x$ and Co@CsPbBr$_3$/TiO$_x$ as photocatalysts, under solar simulator irradiation with the light intensity of 100 mW cm$^{-2}$. b) Yields of reduced and oxidized products with CsPbBr$_3$/TiO$_x$ as the photocatalyst. The error bars are also included in the photocatalytic results from three parallel tests. c) Yields of CO for five consecutive cycles with 3 h each, using CsPbBr$_3$/TiO$_x$ as the photocatalyst.

are 32.4 ± 1.6 and 55.2 ± 1.5 μmol g$^{-1}$ h$^{-1}$, which are manifestly lower than that of CsPbBr$_3$/TiO$_x$ with nanoscale Janus configuration. Transient PL measurements (Figure 3f) revealed that the PL average lifetimes (Table S2, Supporting Information) of CsPbBr$_3$:TiO$_2$ (12.67 ns) and CsPbBr$_3$:USGO:TiO$_2$ (9.14 ns) are noticeably longer compared with that of CsPbBr$_3$/TiO$_x$ (1.08 ns), indicating that the interfacial electron transfer in CsPbBr$_3$/TiO$_x$ is significantly more rapid than those in CsPbBr$_3$:TiO$_2$ and CsPbBr$_3$:USGO:TiO$_2$. Meanwhile, the oxidation product O$_2$ of CsPbBr$_3$/TiO$_x$ can also be detected with an average yield of 53.5 ± 3.5 μmol g$^{-1}$ h$^{-1}$ (Figure 5b), which is almost stoichiometric ratio of 1:2 with respect to the yield of CO. In addition, the photocatalytic stability of CsPbBr$_3$/TiO$_x$ was also estimated by cycling tests (see details in the Supporting Information). As shown in Figure 5c, the drop percentage of CO generation rate is <10% after five cycles, indicating a good stability of CsPbBr$_3$/TiO$_x$ in the gas–solid reaction system. Further XRD, TEM, and XPS measurement confirmed that the crystal structure, morphology, and chemical state of the perovskite of CsPbBr$_3$/TiO$_x$ remained well after the photocatalytic reaction (Figures S14–S16, Supporting Information). Moreover, considering that doping active metal ion in halide perovskite nanocrystals can promote the catalytic activity for CO$_2$ reduction by improving charge separation efficiency and increasing the catalytic sites,[31] we also synthesized a cobalt doped CsPbBr$_3$/TiO$_x$ nanoparticle (coded as Co@CsPbBr$_3$/TiO$_x$, see details in the Supporting Information, Figure S17, Supporting Information). The photocurrent response and EIS measurements (Figure S13, Supporting Information) concurrently indicated that the doping of cobalt can further improve the separation efficicecy of photogenerated carriers. The average CO generation rate of Co@CsPbBr$_3$/TiO$_x$ can reach up to 202.6 ± 2.8 μmol g$^{-1}$ h$^{-1}$, which is more than an order of magnitude higher than those of individual CsPbBr$_3$ and TiO$_x$ as well as CsPbBr$_3$:TiO$_x$ composite, and the external quantum efficiency (EQE) up to 0.22% at 365 nm (Table S4, Supporting Information). At the same time, the oxidation product O$_2$ with stoichiometric ratio can also be detected (Figure S18). The corresponding electron consumption rate ($R_{electron}$) can be calculated as high as 405.2 ± 5.6 μmol g$^{-1}$ h$^{-1}$, far surpassing the reported halide perovskite-based photocatalysts without organic sacrificial agents using the light intensity of 100 mW cm$^{-2}$ (Table S1, Supporting Information).

Control experiments were further performed to identify the sources of CO and O$_2$ with CsPbBr$_3$/TiO$_x$ as photocatalyst. As illustrated in Figure S19, there are no products can be detected in the absence of light irradiation or photocatalyst, indicating the reduction reaction of CO$_2$ is triggered by light over the photocatalyst. Control experiment in the absence of water vapor also shows negligible generation of CO, indicating the electron source of CO$_2$ photoreduction comes from water oxidation. These inferences can be confirmed by further isotopically labeled $^{13}CO_2$ and $H_2{}^{18}O$ experiments. The results of mass spectrometry analyses on the products (Figure S20, Supporting Information) show the distinct signals at $m/z$ = 29 corresponded to $^{13}CO$ and $m/z$ = 36 belonged to $^{18}O_2$, proving that the CO and O$_2$ products were exactly derived from CO$_2$ photoreduction and water oxidation, respectively.

### 2.4. Photocatalytic Mechanism of Z-Scheme Mode

Considering the staggered band structure configuration between CsPbBr$_3$ and TiO$_x$ (Figure 3d), there are two possibilities for the interfacial charge transfer pathway between

$CsPbBr_3$ and $TiO_x$ under the irradiation, which are commonly referred as double-charge transfer (Figure S21, Supporting Information) and direct Z-scheme (Scheme 1a) mechanisms. To ascertain which of these two modes is preferred for the photogenerated carriers in $CsPbBr_3/TiO_x$, the semiconductor properties of as-prepared $CsPbBr_3$ and $TiO_x$ were first investigated by constructing their Mott–Schottky plots. As presented in Figure S22, Supporting Information, both $CsPbBr_3$ and $TiO_x$ have positive slopes at different frequencies, indicating that both $CsPbBr_3$ and $TiO_x$ possess *n*-type semiconductor behavior. Therefore, their Fermi level ($E_F$) positions are biased toward the edges of the corresponding conduction bands, which can be determined by the UPS spectrum measurements (Figure 3b–c), locating at –0.04 and 0.75 eV referred to SHE for $CsPbBr_3$ and $TiO_x$, respectively, as illustrated in Figure 3d. The large difference of $E_F$ and close contact between $CsPbBr_3$ and $TiO_x$ for $CsPbBr_3/TiO_x$ heterojunction would bring forth interface-free electron transfer from $CsPbBr_3$ to $TiO_x$ to realize the Fermi level equilibration of the system, leading to the formation of built-in electric field at the interface of the $CsPbBr_3/TiO_x$ heterojunction associated with band bendings[32] as illustrated in **Figure 6**a. Apparently, the resultant built-in electric field and band bending will hinder the photogenerated electron transfer from $CsPbBr_3$ to $TiO_x$, while facilitate the transfer of photoexcited electron in the conduction band of $TiO_x$ to the valence band of $CsPbBr_3$, implying that the direct Z-scheme mechanism could be preferred for the photoinduced interfacial charge transfer in $CsPbBr_3/TiO_x$ heterojunction as depicted in Figure 6a.

To further confirm the direct Z-scheme mode is operative for the photogenerated carrier transfer in $CsPbBr_3/TiO_x$ heterojunction, the electron paramagnetic resonance (EPR) measurements were performed to monitor the production of spin reactive ·OH and $\cdot O_2^-$ species. 5,5-Dimethyl-1-pyrroline *N*-oxide (DMPO) was employed as trapping agent.[33] As presented in Figure 6b, both $TiO_x$ and $CsPbBr_3/TiO_x$ display strong characteristic signals of DMPO–·OH under light irradiation, whereas no distinct signal can be observed in the case of individual $CsPbBr_3$, owing to the insufficient energy of photogenerated holes in the valance band of $CsPbBr_3$ ($E_{VB}$ = 1.73 V versus SHE) for the oxidation of $H_2O$ to ·OH (2.40 V versus SHE). Meanwhile, it is noted that the signal corresponded to DMPO–·OH in the $CsPbBr_3/TiO_x$ is obviously stronger than pristine $TiO_x$, indicating that the photogenerated holes in the $TiO_x$ component of $CsPbBr_3/TiO_x$ are retained rather than transferred to $CsPbBr_3$, and photoinduced electron–hole pairs are effective separated through the electron transfer from the conduction band of $TiO_x$ to the valence band of $CsPbBr_3$. This phenomenon reveals that the as-prepared $CsPbBr_3/TiO_x$ complies with the direct Z-scheme mode rather than the common double-charge transfer mechanism. If $CsPbBr_3/TiO_x$ follows the double-charge transfer pathway (Figure S21, Supporting Information), the photogenerated holes in the valence band of $TiO_x$ will be transferred to the valence band of $CsPbBr_3$, and the DMPO–·OH signal will not be observed because the holes in the valence band of $CsPbBr_3$ do not have the ability to trigger the oxidation of $H_2O$ to ·OH. The efficient photoinduced electron–hole separation in $CsPbBr_3/TiO_x$ can be further confirmed by detecting the DMPO–$\cdot O_2^-$ characteristic peaks

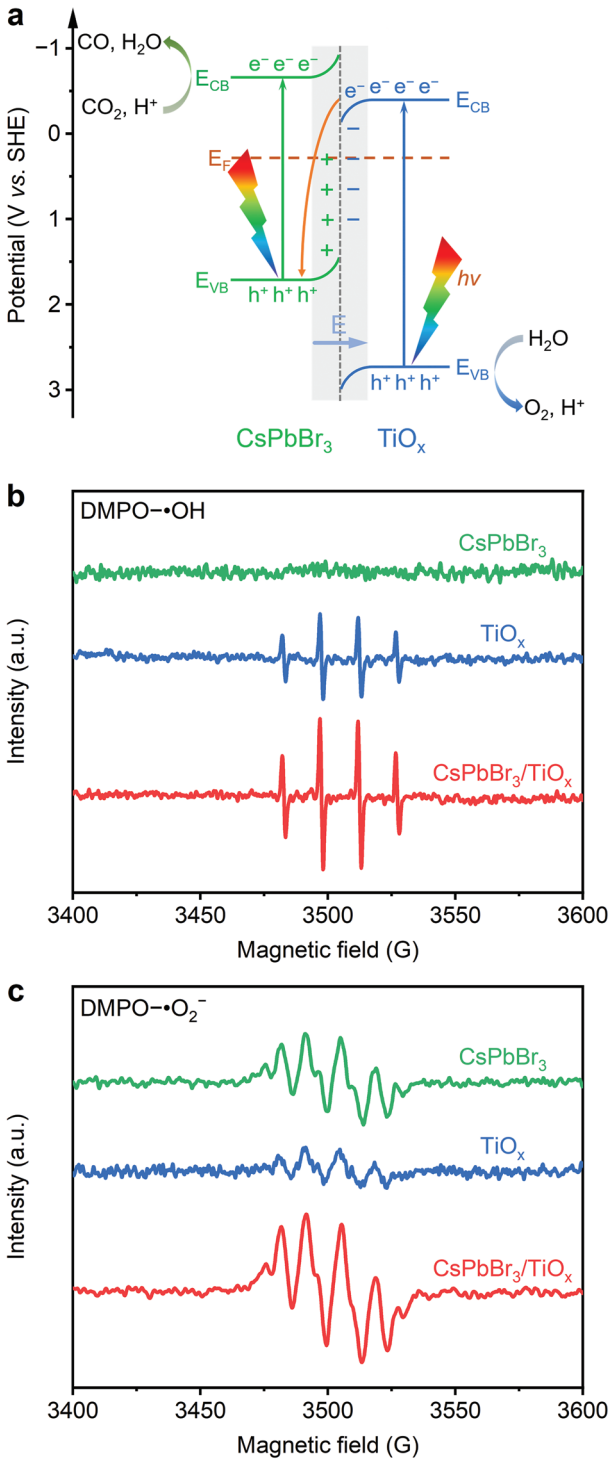


**Figure 6.** a) Energy band structure and schematic illustration of the Z-scheme reaction mechanism of $CsPbBr_3/TiO_x$ heterojunction for photocatalysis of $CO_2$ reduction coupled with water oxidation. EPR spectra of b) DMPO–·OH and c) DMPO–$\cdot O_2^-$ of $TiO_x$, $CsPbBr_3$, and $CsPbBr_3/TiO_x$ under light irradiation.

of $CsPbBr_3$, $TiO_x$, and $CsPbBr_3/TiO_x$. As depicted in Figure 6c, the DMPO–$\cdot O_2^-$ signal generated in the $CsPbBr_3/TiO_x$ are also evidently stronger than those of single $CsPbBr_3$ and $TiO_x$. In

addition, no DMPO–·OH and DMPO–$\cdot O_2^-$ signals can be detected without light irradiation (Figure S23, Supporting Information) for all the samples, confirming that the reactive ·OH and $\cdot O_2^-$ species were generated by photogenerated carriers.

Based on the above results, we can propose the Z-scheme mechanism of $CsPbBr_3/TiO_x$ for photocatalytic $CO_2$ reduction integrated with $H_2O$ oxidation as depicted in Figure 6a. Light irradiation induces the generation of electron–hole pairs in both $CsPbBr_3$ and $TiO_x$. Thereafter, the photogenerated electrons in the conduction band of $TiO_x$ were swiftly transferred to the valence band of $CsPbBr_3$ due to the close contact and the formation of built-in electric field between $CsPbBr_3$ and $TiO_x$, achieving effective spatial separation of photoinduced electron–hole pairs. The retained photogenerated holes in $TiO_x$ with strong oxidation capability ($E_{VB}$ = 2.74 V versus SHE) are able to oxidize $H_2O$ to generate $O_2$ and $H^+$ ($4h^+ + 2H_2O \rightarrow O_2 + 4H^+$, 1.23 V versus SHE).[34] Meanwhile, $CsPbBr_3$ with strongly reductive electrons ($E_{CB}$ = –0.63 V versus SHE) will trigger the $CO_2$ reduction to CO following the two-electron and two-proton process ($CO_2 + 2e^- + 2H^+ \rightarrow CO + H_2O$, –0.12 V versus SHE).[34] Thereby, the effective separation of photogenerated carriers and preserved strong reduction and oxidation capacities in $CsPbBr_3/TiO_x$ are mainly responsible for the significantly enhanced photocatalytic performance for $CO_2$ reduction coupled with $H_2O$ oxidation.

## 3. Conclusion

In summary, a MHP-based nanoscale Janus Z-scheme heterojunction of $CsPbBr_3/TiO_x$ has been controllably synthesized by a facile interfacial synthesis strategy, which shows outstanding photocatalytic activity for overall reaction of artificial photosynthesis. The short carrier transport distance and direct contact between $CsPbBr_3$ and $TiO_x$ NCs endows $CsPbBr_3/TiO_x$ heterojunction with swift interfacial charge transfer following a Z-scheme mode, as demonstrated by steady-state and transient PL, SPV, photoelectrochemical, UPS and EPR measurements. Benefitting from the efficient spatial separation at the nanoscale and preserved strong redox potentials of photogenerated carriers, the photocatalytic $CO_2$ reduction performance of $CsPbBr_3/TiO_x$ significantly transcends those of $CsPbBr_3$ and $CsPbBr_3$:$TiO_x$. The strategy presented here for the construction of isolated Z-scheme heterojunction at the nanoscale with swift interfacial charge transfer could be extended to other semiconductor-based photocatalysts, providing a new avenue for the development of efficient artificial photosynthesis photocatalysts.

## Supporting Information

Supporting Information is available from the Wiley Online Library or from the author.

## Acknowledgements

This work was financially supported by the National Key R&D Program of China (2022YFA1502902 and 2017YFA0700104), NSFC (21931007, 21790052 and U21A20286), Natural Science Foundation of Tianjin City (17JCJQJC43800), and the 111 Project of China.

## Conflict of Interest

The authors declare no conflict of interest.

## Data Availability Statement

The data that support the findings of this study are available from the corresponding author upon reasonable request.;

## Keywords

charge transfer, $CO_2$ reduction, nanoscale Janus heterojunction, perovskite nanocrystals, photocatalysis

Received: February 10, 2023
Revised: March 12, 2023
Published online:

[1] a) W. Gao, S. Liang, R. Wang, Q. Jiang, Y. Zhang, Q. Zheng, B. Xie, C. Y. Toe, X. Zhu, J. Wang, L. Huang, Y. Gao, Z. Wang, C. Jo, Q. Wang, L. Wang, Y. Liu, B. Louis, J. Scott, A. C. Roger, R. Amal, H. Heh, S. E. Park, *Chem. Soc. Rev.* **2020**, *49*, 8584; b) T. A. Jacobson, J. S. Kler, M. T. Hernke, R. K. Braun, K. C. Meyer, W. E. Funk, *Nat. Sustain.* **2019**, *2*, 691.
[2] O. S. Bushuyev, P. De Luna, C. T. Dinh, L. Tao, G. Saur, J. Van De Lagemaat, S. O. Kelley, E. H. Sargent, *Joule* **2018**, *2*, 825.
[3] T. Inoue, A. Fujishima, S. Konishi, K. Honda, *Nature* **1979**, *277*, 637.
[4] T. Wang, J. Gong, *Nat. Energy* **2020**, *5*, 642.
[5] a) Y. Pellegrin, F. Odobel, *C. R. Chim.* **2017**, *20*, 283; b) H. Rao, L. C. Schmidt, J. Bonin, M. Robert, *Nature* **2017**, *548*, 74; c) Q. Guo, F. Liang, X. B. Li, Y. J. Gao, M. Y. Huang, Y. Wang, S. G. Xia, X. Y. Gao, Q. C. Gan, Z. S. Lin, C. H. Tung, L. Z. Wu, *Chem* **2019**, *5*, 2605; d) F. Arcudi, L. Đorđević, B. Nagasing, S. I. Stupp, E. A. Weiss, *J. Am. Chem. Soc.* **2021**, *143*, 18131.
[6] S. Ye, C. Ding, M. Liu, A. Wang, Q. Huang, C. Li, *Adv. Mater.* **2019**, *31*, 1902069.
[7] a) Z. Jiang, X. Xu, Y. Ma, H. S. Cho, D. Ding, C. Wang, J. Wu, P. Oleynikov, M. Jia, J. Cheng, Y. Zhou, O. Terasaki, T. Peng, L. Zan, H. Deng, *Nature* **2020**, *586*, 549; b) S. Kreft, R. Schoch, J. Schneidewind, J. Rabeah, E. V. Kondratenko, V. A. Kondratenko, H. Junge, M. Bauer, S. Wohlrab, M. Beller, *Chem* **2019**, *5*, 1818; c) H. Huang, J. Lin, G. Zhu, Y. Weng, X. Wang, X. Fu, J. Long, *Angew. Chem., Int. Ed.* **2016**, *55*, 8314.
[8] K. L. Bae, J. Kim, C. K. Lim, K. M. Nam, H. Song, *Nat. Commun.* **2017**, *8*, 1156.
[9] R. Li, W. H. Cheng, M. H. Richter, J. S. DuChene, W. Tian, C. Li, H. A. Atwater, *ACS Energy Lett.* **2021**, *6*, 1849.
[10] Q. Han, X. Bai, Z. Man, H. He, L. Li, J. Hu, A. Alsaedi, T. Hayat, Z. Yu, W. Zhang, J. Wang, Y. Zhou, Z. Zou, *J. Am. Chem. Soc.* **2019**, *141*, 4209.
[11] Y. A. Wu, I. McNulty, C. Liu, K. C. Lau, Q. Liu, A. P. Paulikas, C. J. Sun, Z. Cai, J. R. Guest, Y. Ren, V. Stamenkovic, L. A. Curtiss, Y. Liu, T. Rajh, *Nat. Energy* **2019**, *4*, 957.
[12] J. Wu, X. Li, W. Shi, P. Ling, Y. Sun, X. Jiao, S. Gao, L. Liang, J. Xu, W. Yan, C. Wang, Y. Xie, *Angew. Chem., Int. Ed.* **2018**, *57*, 8719.

[13] a) W. Tu, Y. Zhou, Z. Zou, *Adv. Mater.* **2014**, *26*, 4607; b) X. Liu, S. Inagaki, J. Gong, *Angew. Chem., Int. Ed.* **2016**, *55*, 14924.
[14] a) W. Zhang, A. R. Mohamed, W. J. Ong, *Angew. Chem., Int. Ed.* **2020**, *59*, 22894; b) Q. Xu, L. Zhang, B. Cheng, J. Fan, J. Yu, *Chem* **2020**, *6*, 1543; c) Q. Wang, J. Warnan, S. Rodríguez-Jiménez, J. J. Leung, S. Kalathil, V. Andrei, K. Domen, E. Reisner, *Nat. Energy* **2020**, *5*, 703; d) E. M. Akinoglu, D. A. Hoogeveen, C. Cao, A. N. Simonov, J. J. Jasieniak, *ACS Nano* **2021**, *15*, 7860; e) M. Zhang, M. Lu, Z. L. Lang, J. Liu, M. Liu, J. N. Chang, L. Y. Li, L. J. Shang, M. Wang, S. L. Li, Y. Q. Lan, *Angew. Chem., Int. Ed.* **2020**, *59*, 6500; f) D. Li, J. Zhou, Z. Zhang, Y. Jiang, Z. Dong, J. Xu, C. Yao, *ACS Appl. Energy Mater.* **2022**, *5*, 6238.
[15] H. Hu, L. Wu, Y. Tan, Q. Zhong, M. Chen, Y. Qiu, D. Yang, B. Sun, Q. Zhang, Y. Yin, *J. Am. Chem. Soc.* **2018**, *140*, 406.
[16] N. G. Park, K. Zhu, *Nat. Rev. Mater.* **2020**, *5*, 333.
[17] X. K. Liu, W. Xu, S. Bai, Y. Jin, J. Wang, R. H. Friend, F. Gao, *Nat. Mater.* **2021**, *20*, 10.
[18] Q. A. Akkerman, G. Rainò, M. V. Kovalenko, L. Manna, *Nat. Mater.* **2018**, *17*, 394.
[19] a) Z. Zhang, Y. Jiang, M. Shu, L. Li, Z. Dong, J. Xu, *J. Phys. Chem. Lett.* **2021**, *12*, 5864; b) H. Huang, B. Pradhan, J. Hofkens, M. B. J. Roeffaers, J. A. Steele, *ACS Energy Lett.* **2020**, *5*, 1107; c) J. Chen, C. Dong, H. Idriss, O. F. Mohammed, O. M. Bakr, *Adv. Energy Mater.* **2020**, *10*, 1902433; d) H. L. Wu, X. B. Li, C. H. Tung, L. Z. Wu, *Adv. Mater.* **2019**, *31*, 1900709; e) Q. M. Sun, J. J. Xu, F. F. Tao, W. Ye, C. Zhou, J. H. He, J. M. Lu, *Angew. Chem., Int. Ed.* **2022**, *61*, e202200872; f) S. Bera, S. Shyamal, N. Pradhan, *J. Am. Chem. Soc.* **2021**, *143*, 14895; g) Z. Chen, Y. Hu, J. Wang, Q. Shen, Y. Zhang, C. Ding, Y. Bai, G. Jiang, Z. Li, N. Gaponik, *Chem. Mater.* **2020**, *32*, 1517; h) F. Xu, K. Meng, B. Cheng, S. Wang, J. Xu, J. Yu, *Nat. Commun.* **2020**, *11*, 4613; i) H. Huang, J. Zhao, Y. Du, C. Zhou, M. Zhang, Z. Wang, Y. Weng, J. Long, J. Hofkens, J. A. Steele, M. B. J. Roeffaers, *ACS Nano* **2020**, *14*, 16689; j) J. Wang, J. Wang, N. Li, X. Du, J. Ma, C. He, Z. Li, *ACS Appl. Mater. Interfaces* **2020**, *12*, 31477; k) Y. F. Mu, W. Zhang, G. X. Dong, K. Su, M. Zhang, T. B. Lu, *Small* **2020**, *16*, 2002140; l) Y. Jiang, J. F. Liao, H. Y. Chen, H. H. Zhang, J. Y. Li, X. D. Wang, D. B. Kuang, *Chem* **2020**, *6*, 766; m) L. Y. Wu, Y. F. Mu, X. X. Guo, W. Zhang, Z. M. Zhang, M. Zhang, T. B. Lu, *Angew. Chem., Int. Ed.* **2019**, *58*, 9491; n) M. Ou, W. Tu, S. Yin, W. Xing, S. Wu, H. Wang, S. Wan, Q. Zhong, R. Xu, *Angew. Chem., Int. Ed.* **2018**, *57*, 13570; o) Y. F. Xu, M. Z. Yang, B. X. Chen, X. D. Wang, H. Y. Chen, D. B. Kuang, C. Y. Su, *J. Am. Chem. Soc.* **2017**, *139*, 5660.
[20] L. Wu, H. Hu, Y. Xu, S. Jiang, M. Chen, Q. Zhong, D. Yang, Q. Liu, Y. Zhao, B. Sun, Q. Zhang, Y. Yin, *Nano Lett.* **2017**, *17*, 5799.
[21] Z. J. Li, E. Hofman, J. Li, A. H. Davis, C. H. Tung, L. Z. Wu, W. Zheng, *Adv. Funct. Mater.* **2018**, *28*, 1704288.
[22] a) Y. Yu, D. Zhang, C. Kisielowski, L. Dou, N. Kornienko, Y. Bekenstein, A. B. Wong, A. P. Alivisatos, P. Yang, *Nano Lett.* **2016**, *16*, 7530; b) Z. Dang, J. Shamsi, F. Palazon, M. Imran, Q. A. Akkerman, S. Park, G. Bertoni, M. Prato, R. Brescia, L. Manna, *ACS Nano* **2017**, *11*, 2124.
[23] Z. Wang, C. Yang, T. Lin, H. Yin, P. Chen, D. Wan, F. Xu, F. Huang, J. Lin, X. Xie, M. Jiang, *Adv. Funct. Mater.* **2013**, *23*, 5444.
[24] Y. F. Xu, X. D. Wang, J. F. Liao, B. X. Chen, H. Y. Chen, D. B. Kuang, *Adv. Mater. Interfaces* **2018**, *5*, 1801015.
[25] H. Chen, A. Guo, J. Zhu, L. Cheng, Q. Wang, *Appl. Surf. Sci.* **2019**, *465*, 656.
[26] M. S. Lazarus, T. K. Sham, *Chem. Phys. Lett.* **1982**, *92*, 670.
[27] K. Su, G. X. Dong, W. Zhang, Z. L. Liu, M. Zhang, T. B. Lu, *ACS Appl. Mater. Interfaces* **2020**, *12*, 50464.
[28] L. Zhang, J. Ran, S. Z. Qiao, M. Jaroniec, *Chem. Soc. Rev.* **2019**, *48*, 5184.
[29] H. Abdullah, M. M. R. Khan, H. R. Ong, Z. Yaakob, *J. CO2 Util.* **2017**, *22*, 15.
[30] Y. F. Mu, C. Zhang, M. R. Zhang, W. Zhang, M. Zhang, T. B. Lu, *ACS Appl. Mater. Interfaces* **2021**, *13*, 22314.
[31] a) J. Cheng, Y. Mu, L. Wu, Z. Liu, K. Su, G. Dong, M. Zhang, T. Lu, *Nano Res.* **2022**, *15*, 1845; b) J. Ran, M. Jaroniec, S. Z. Qiao, *Adv. Mater.* **2018**, *30*, 1704649.
[32] Z. Zhang, J. T. Yates, *Chem. Rev.* **2012**, *112*, 5520.
[33] W. Shi, F. Guo, S. Yuan, *Appl. Catal. B* **2017**, *209*, 720.
[34] P. D. Tran, L. H. Wong, J. Barber, J. S. C. Loo, *Energy Environ. Sci.* **2012**, *5*, 5902.